Kurdish Studies
Apr 2023
Volume: 11, No: 02, pp. 1493-1508
ISSN: 2051-4883 (Print) | ISSN 2051-4891 (Online)
www.KurdishStudies.net

Received: May 2023 Accepted: June 2023
DOI: https://doi.org/10.58262/ks.v11i02.103

Gain Enhancement of Electronically Steered Dual-Beam Antenna Using Metamaterial Radome

Auychai Yatongchai[1], Peerasan Khamsalee[2], Rangsan Wongsan[3]

Abstract

The dual-beam steering antenna is a PCB-based circular patch antenna design for dual-beam steering, utilizing super-substrate multi-layer metamaterial radomes by stacking techniques of five metamaterial radomes. This design employs the original circular patch antenna, which consists of eight small square patches placed symmetrically at eight angles and separated by slots. The beam-steering property of this antenna can be implemented by controlling the on/off state of the PIN diodes, which are connected between each small square patch and main patch at each angle of the structure. The gain enhancement achieved using the metamaterial radomes uses a combination of Jerusalem cross-frequency selective surface and Square loop-frequency selective surfaces unit cells arranged in a 4×4 array. There are five layers, and each layer's distance depends on the wavelength, affects the gain, and efficiency improvement of the antenna with metamaterial radomes can be increased to at least 3 dB, radiating the waves for longer distances and covering more space.

Keywords: *Beam-steering, Dual-beam, PIN-diode, Metamaterial, Meta-radome*

Introduction

In recent years, the use of unmanned aerial vehicles (UAV) has attracted significant interest in the military, communications, and commercial markets. Unmanned aerial vehicles, commonly known as drones, are aircraft without a pilot, crow, or passengers on board, and have become one of the most interesting areas of the Defence Technology Institute (Public Organization) Ministry of Defiance, the Kingdom of Thailand. In addition to the ongoing projects implemented by DTI, a modified anti-aircraft rocket project with a prototype developed into a modified rocket propulsion system and testing to verify the design results is one of the projects of which DTI is proud. This project was integrated into the Department of Royal Rainmaking and Agricultural Aviation. This Project was used to support the Royal Rainmaking Project. It is an extension of the knowledge of rocket production to support projects through royal initiatives and for the defense of the country (Defence Technology Institute, 2016). In Thailand, high-altitude platform stations are to be operated in the frequency spectrum of the C-band and X-band to support operations in fixed and mobile services. The high-altitude platform station is 17 km above the Earth's surface and serves a ground area of 60-200 km in diameter, with an elevation angle from the ground of up to 30 °. "General Use" is meant in accordance with the use purpose of UAV which is externally controlled for aviation as stipulated in the Notification of the Ministry of Transport on Rules for permission and conditions for control and launch of unmanned aircraft in the category of

[1] School of Telecommunication Engineering, Institute of Engineering, Suranaree University of Technology, Nakhon Ratchasima, Thailand. Email: auychai_ya@hotmail.com
Idhttps://ORCIDID.org/: 0009-0004-2150-2445
[2] School of Telecommunication Engineering, Institute of Engineering, Suranaree University of Technology, Nakhon Ratchasima, Thailand. Email: mpeerasan.k@gmail.com
[3] School of Telecommunication Engineering, Institute of Engineering, Suranaree University of Technology, Nakhon Ratchasima, Thailand. Email: rangsan@sut.ac.th

remotely piloted aircraft and subsequent amendment. The use of radio frequency and equivalent isotropically radiated power (e. i. r. p.) are determined at 5.725–5.850 GHz and 1000 mW, respectively (Government Gazette, 2018; Muhammad et al., 2011). The antennas commonly used with UAVs are dipoles, patches, arrays, skew plannas, and helical antennas, which are omnidirectional and single-beam directional antennas, which generally have a gain of about 4 dB - 7 dB (Zhang, & Yang, 2017; Zhang Wei & Yang, 2018; Xinhuan, et al.,2021). An interesting antenna that Muhammad Ezanuddin has designed is a dual beam antenna using metamaterial based on a complementary split ring resonator, mounted on both wings of the aircraft. which the antenna provides a gain of ~7 dB (Muhammad et al., 2011). Therefore, researchers are interested in the design of beam-steering antennas to compensate for blind angles from aerobatic flight, increased gain, and radiated waves for longer distances and to cover more space.

Recently, beam-steering antennas have become one of the most interesting areas of wireless communication, especially antennas for future high-altitude platforms such as drones, missiles, and aircraft. The beam-steering antenna on such platforms can be continuously tracked and commanded from their control stations within a specific distance without disconnection. At present, there are various techniques for steering antenna beams, such as the use of switchable parasitic elements, leaky-wave antennas on PCB, comb line techniques on microstrip arrays, and steerable beams with metamaterial structures (Camblor, 2010; Jais et al., 2013; Iyemeh & James, 2016; Hisamatsu, 2017; Asaduzzaman et al, 2018). In this study, we focus on a PCB-based microstrip patch antenna owing to its simple structure, ease of fabrication, light weight, and low cost. To steer the beam of this antenna, beam steering can be implemented by controlling the on/off state of the PIN diodes, which are connected to a small square patch of the structure. When the diode is on, the small square patch becomes part of the radiating patch, whereas is off and the small square patch becomes a parasitic element. If we can design an electronically steered dual-beam antenna, the switching beam can be decreased by half compared to that of a conventional single-beam antenna to reduce the signal loss during switchover. An electronically steered dual-beam antenna with a metamaterial-based radome was presented theoretically.

Subsequently, the influence of the dimensions and positions of the small square patch was described. When these parameters were found, eight elements of the small square patch addition and microstrip patches were investigated to meet the requirements of the proposed dual beam. The simulation results obtained using CST software show the curves of the reflection characteristics, S_{11} of the patch antenna, and dual beam, which can be improved by varying the number and dimension of the small square patches.

In this study, a method to increase the efficiency of antennas using a new technology called metamaterial structure is proposed because it can increase the radiation efficiency of microwave antennas (Engheta et al, 2006; Yang, & Rahmatsamii, 2009). In addition, the design of the metamaterial-based radome covering the electronically steered dual-beam antenna protected the antenna effect from the environment, and the antenna gain could be increased to at least 3 dB, radiating the waves for longer distances and covering more space. Finally, the experimental results of the dual-beam steering were measured and validated with the simulation results.

Theory and Configuration of the Proposed Antenna

Circular Patch Design Method

Initially, suitable and similar substrates must be selected to provide a common platform for antenna simulations. This greatly reduces any discrepancies, instead of simulating the fabrication of different microwave laminates. The chosen substrate has a dielectric constant (ε_r), dielectric loss tangent ($tan\delta$),

and substrate height *(h)* for a single layer. The patch width should be selected to obtain a good radiation efficiency if the real estate requirements or grating lobe are not overriding factors. It has been suggested that $1< W/L < 2$, for an operating frequency 5.8 GHz. The width of the TM_{10} Mode was given by (Balanis, 2005).

$$W = \frac{1}{2f_r\sqrt{\mu_0\varepsilon_0}}\sqrt{\frac{2}{\varepsilon_r+1}} = \frac{v_0}{2f_r}\sqrt{\frac{2}{\varepsilon_r+1}} \quad (1)$$

where ε_r is the relative dielectric constant, ε_0 is the free-space permittivity, μ_0 is the permeability of air, f_r is the resonant frequency, and v_0 is the speed of light in the free space.

The length of the patch determines the resonant frequency and is an important design parameter owing to its inherently narrow bandwidth. The extended incremental length of patch ΔL is.

$$\frac{\Delta L}{h} = 0.412\left[\frac{(\varepsilon_{reff}+1)\left(\frac{W}{h}+0.264\right)}{(\varepsilon_{reff}-0.258)\left(\frac{W}{h}+0.8\right)}\right] \quad (2)$$

Thus, the actual length of the patch is;

$$L = \frac{\lambda}{2} - 2\Delta L \quad (3)$$

The conversion from a common rectangular shape to a circular shape is given by the following equation: $A_{rectangular}$ $(width \times length) = A_{circular}$ (πr^2); The diagram is shown in Figure 1(a).

Figure 1: Shows (a) Diagram of changing rectangular shape to circular shape and (b) the geometry of

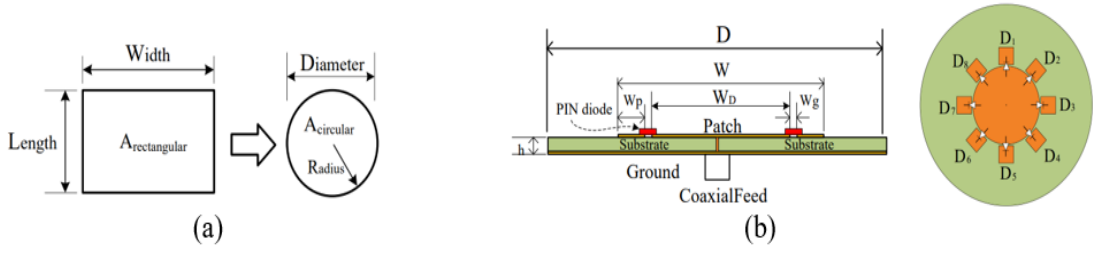

proposed slit-top uniform square patch and circular patch.

There are several types of beam-steering antennas such as patches, circular plates, SRRs, and cross-shaped structures (Hisamatsu et al., 2017; Jais, 2013). We chose square and circular patches in the current design because of their simplicity and symmetrical geometry for supporting the dual beam. Figure 1(b) shows the slit-top uniform square patch and its dimensions. The microstrip patch antenna's parameters are as follows: D = 75 mm, w_p = 5.6 mm, w_g = 0.4 mm, W_D = 38 mm, h = 1.6 mm, ε_r = 4.4, and loss tangent $tan\delta$ = 0.025.

Bias T (Bias Tee) and PIN Diode Circuits for Controlled Dual Beam Antennas

Bias T is a special 3-port device that is mainly used when trying to use DC power (DC Bias) to protect RF components from being damaged by DC bias. L_1 and L_2 prevent the reverse current of the RF signal while the PIN diode is biased (see Figure 2). A typical Bias T circuit looks like this: to see the circuit is 'T' shaped, which is why it is called bias T. A PIN diode was used to switch the active frequency selective surface transmission on and off at 5.8 GHz. Description of the SMP1345 chip package. This PIN diode is designed for high-throughput devices such as wireless local area networks (WLAN), low-noise blocks (LNB), and switch applications from 10 MHz to 6 GHz. The short carrier lifetime is typically 100 ns (typical), combined with an I-region width as thin as 10 μm (nominal), resulting in a group of high-speed RF-switching PIN diodes. The SMP1345 series exhibited RF performance because of its very low capacitance (0.15 pF) and impedance (1.5 Ω at 10 mA).

Figure 2: Bias tee and PIN diode circuits.

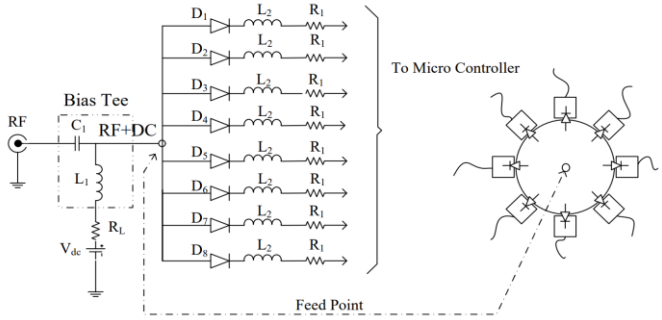

Theory and Configuration of the Meta Radome

Equivalent circuit model of combined JC-FSS with conventional SL-FSS

This section explains the understanding of equivalent circuits and their parameters of the unit cells, which are described by combining the two types of unit cells. The equivalent circuits of the conventional SL-FSSs were defined as the values of the terms seen in Figure 3 were derived in (Parker, 1991). The admittance and impedance of the SL-FSS can be calculated using the equivalent circuit shown in Figure 3 given by Parker (1991).

$$Z_{01} = j(\omega L_1 - (1/\omega C_1)) \quad = \quad \frac{-j}{\omega C_1}(1 - \omega^2 L_1 C_1) \quad (4)$$

$$Y_1 = \frac{1}{Z_{01}} = \frac{1}{\frac{-j}{\omega C_1}(1-\omega^2 L_1 C_1)} = \frac{j\omega C_1}{-j^2(1-\omega^2 L_1 C_1)} = j\left(\frac{\omega C_1}{(1-\omega^2 L_1 C_1)}\right) \quad ; j^2 = -1 \quad (5)$$

Figure 3: The band stop equivalent circuit of three SL-FSSs structure

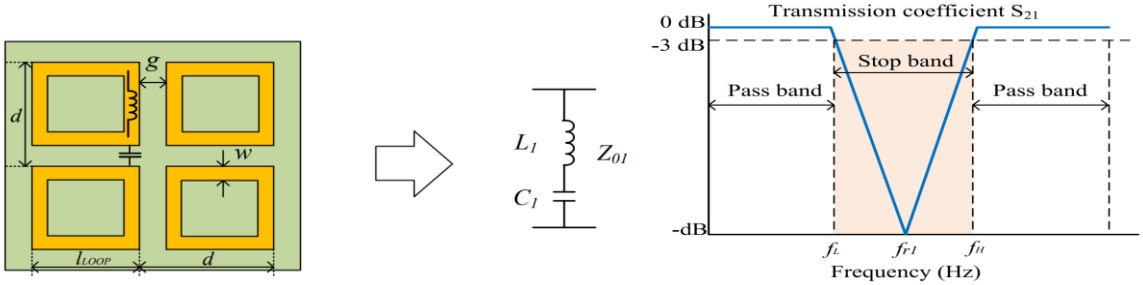

In general, in the basic structures of frequency-selective surfaces (FSS), these metallic arrays may exist in a homogeneous medium or at the interface of two different dielectric substrates. Based on (Yuan, & Mang, 2019), the characteristics of the lumped equivalent circuit of the SL-FSS structures is the band-stop filter shown in Figure 3 were derived. This is a lumped element used to analyze the surface impedance formula. Yuan and Mang (2019) described the method for estimating the per-unit-length inductance (L_1) of the strip in the SL-FSS structure and the per-unit-length capacitance (C_1) of the slot between two adjacent patches in the SL-FSS structure. It can be estimated using Equations (6) and (7) as follows:

$$L_1 = \mu_0 \frac{l_{Loop}}{2\pi} ln\left(1/\sin\left(\frac{\pi w}{2d}\right)\right) \quad (6)$$

$$C_1 = \varepsilon_0 \varepsilon_{reff} \frac{2l_{Loop}}{\pi} ln\left(1/\sin\left(\frac{\pi g}{2d}\right)\right) \quad (7)$$

Where the resonant frequency (f_r) can be expressed as the following equation:

$$f_{r1} = \frac{1}{(2\pi\sqrt{C_1 L_1})} \quad (8)$$

where $g = (d - l_{Loop})$ is the slot width and w is the strip width, as shown in Figure 3. L_1 and C_1 represent the inductance and capacitance of the equivalent circuit model of the SL-FSS array, respectively.

Figure 4: Shows the equivalent circuit of (a) the surface impedance, and (b) the model of JC-FSS array.

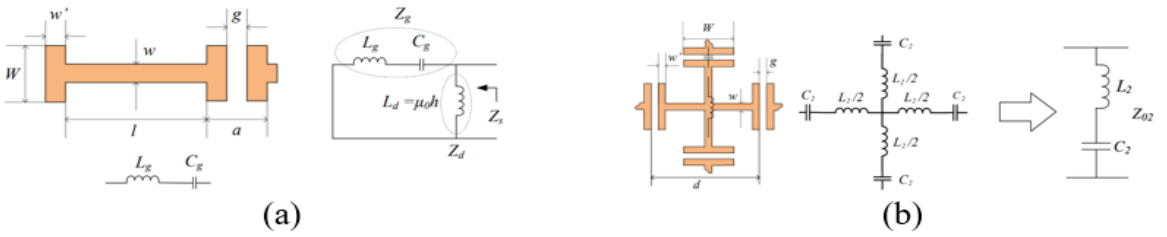

Consider the geometry of a Jerusalem cross-frequency selective surface (JC-FSS) with a cross-shaped metal plate on a dielectric substrate. The JC-FSS element and ground plane are considered perfectly conductive when the period is small compared to the wavelength of interest. The equivalent circuit and characteristics of the artificial magnetic conductor (AMC) can be described using the effective surface impedance model shown in Figure 4(a). The JC-FSS equivalent circuit in Figure 4(b) is the configured band-stop filter, where C_2 is the capacitance C_g and L_2 is the sum of the inductances L_s and L_d.

When the AMC structure has an important parameter, the surface impedance (Z_s) plays an important role in determining the resonance frequency and the phase of the reflection coefficient. The surface impedance (Z_s) can be taken in a transmission line approach, explaining that the JC-FSS impedance (Z_g) and the surface impedance of the grounded dielectric slab (Z_d) are connected in parallel (Hosseini, & Hakkak, 2008). Therefore, in Figure 4, the surface impedance can be expressed as.

$$Z_s(\omega) = Z_g \| Z_d = j\omega L_d \frac{1-\omega^2 L_g C_g}{1-\omega^2 C_g (L_d + L_g)} \quad (9)$$

In Equation (9), ω is the angular frequency, L_d is the inductance of the grounded dielectric slab, and L_g is the inductance of the JC-FSS. Where C_g is the capacitance formed by the adjacent JC-FSS junction, which has very little influence on Z_d. When the denominator of Equation (9) is equal to zero, the resonant frequency (f_r) can be expressed as the following equation:

$$f_{r2} = \frac{1}{2\pi\sqrt{C_2 L_2}} = \frac{1}{2\pi\sqrt{C_g (L_g + L_d)}} \quad (10)$$

Therefore, Z_s is very high and the reflection phase coefficient is zero at the resonant frequency (f_r).

In (Sievenpiper, 1999), a simple estimation method for determining capacitance C_g, Sievenpiper described an approach to extract the capacitance of two parallel patches placed on a dielectric slab.

$$C_g = \frac{2W}{\pi} \varepsilon_0 \varepsilon_{reff} \, Cosh^{-1}\left(\frac{a}{g}\right) \quad (11)$$

The inductive component (L_g) is the length of l, the width of w using the microstrip transmission line theory, and c is the velocity of light in free space, which can be estimated using the formula (Bahl, 2003):

$$L_g = \frac{Z_0 \sqrt{\varepsilon_{reff}}}{c} l \quad (12)$$

When, the effective dielectric constant can be calculated using equation (13) (Gupta, 1996).

$$\varepsilon_{reff} = \frac{\varepsilon_r+1}{2} + \frac{\varepsilon_r-1}{2}\left(1+\frac{12h}{w}\right)^{-\frac{1}{2}} + 0.041\left(1-\frac{w}{h}\right)^2 \quad ;\frac{w}{h} \leq 1 \quad (13)$$

where h is the thickness of the dielectric slab, w is the width of the microstrip line, and η is the impedance of the free space. L_2 and C_2 represent the inductance and capacitance of the equivalent circuit model of the JC-FSS array theory, respectively, as shown in Figure 4(b), which was described by (Pristin, 2013; Anderson, 1975), Z_0 and Y_2 are described by Equation (14)–(15), respectively.

$$Z_{02} = j\left(\omega L_2 - (1/\omega C_2)\right) \quad (14)$$

$$Y_2 = j\left(\frac{\omega C_2}{(1-\omega^2 L_2 C_2)}\right) \quad (15)$$

The inductance of a grounded dielectric slab is an incident wave normal to the surface of the JC AMC, and the impedance of a metal-backed dielectric slab with thickness h can be expressed as (Simovski et al., 2005).

$$Z_d = \left(\frac{j\eta}{\sqrt{\varepsilon_r}}\right) tan\ kh \quad (16)$$

In Figure 4(a), Z_d is modeled by inductance (L_d). We have $Z_d = j\omega L_d$; therefore, we can write it immediately as follows:

$$L_d = \left(\frac{\eta}{(\omega\sqrt{\varepsilon_r})}\right) tan\ kh \quad (17)$$

where $k = \omega\sqrt{\varepsilon_r \varepsilon_0 \mu_0}$ is the wave number and $\eta = \sqrt{\mu_0 / \varepsilon_0}$ is the free-space impedance

Figure 5: Shows (a) To combined JC- FSS with conventional SL-FSS, and (b) the dual-band stop filter equivalent circuits model of JC-FSS with SL-FSS.

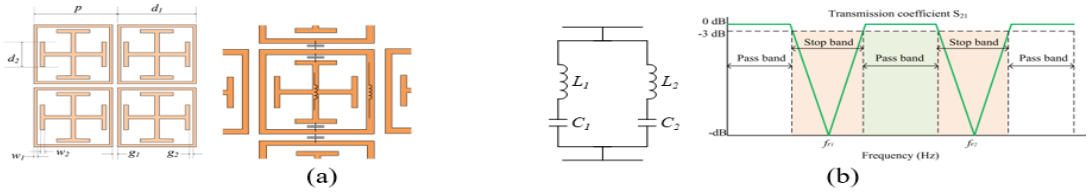

Finally, Figure 5(a) shows the geometry and dimensions of the combined JC-FSS with the conventional SL-FSS for the design unit cell, and the admittance of the combined JC-FSS with the conventional SL-FSS is calculated using the $L_1C_1//L_2C_2$ equivalent circuit as a dual-band stop, where a pass band appears between the two band stops, as shown in Figure 5(b).

$$Y = Y_1 + Y_2 = \left(j\frac{\omega C_1}{(1-\omega^2 C_1 L_1)} + j\frac{\omega C_2}{(1-\omega^2 C_2 L_2)}\right) = j\omega\left(\frac{C_1+C_2-\omega^2 C_1 C_2 (L_1+L_2)}{(1-\omega^2 C_1 L_1)(1-\omega^2 C_2 L_2)}\right) \quad (18)$$

We define C_1 and L_1 as the capacitance and inductance of the SL-FSS equivalent circuit, respectively, and C_2 and L_2 are the capacitance and inductance of the JC-FSS equivalent circuit, respectively. Therefore, we can estimate Z_0 from the LC parallel equivalent circuit from the $Z_{LC\|LC} = 1/Y$ using Equation (18).

$$Z_{LC||LC} = \frac{1}{Y} = \frac{1}{j\omega}\left(\frac{(1-\omega^2 C_1 L_1)(1-\omega^2 C_2 L_2)}{C_1+C_2-\omega^2 C_1 C_2 (L_1+L_2)}\right) \quad (19)$$

Simulation Results of Antenna

shows the simulated results for the reflection performance of the square patch shown in Figure 6 when

its patch width (w_p) is kept constant and the gap width (w_g) is varied. The capacitance ratio is varied, as well as the values of L and C of the gap. As the patch width (w_g) is reduced, the values of L and C decrease, which is assigned to characterize the reflection curve that occurs in the required frequency band. First, in Figure 6(a), the value of w_p is fixed, whereas the value of w_g is varied to determine the proper slit width for the patch. We found that the width of w_g was related to the position of the resonant frequency. In Figure 6(b), to consider the effect of patch width, w_p is varied from 4.5 mm to 6.5 mm while its length (w_g) is fixed at 0.8 mm. It was found that the bandwidth of the passband increased when the width of the patch was enlarged. These properties can be exploited in the design of slit-patch structures to increase frequency response. In Figure 6(c), the effect of the antenna diameter (D) varied from 65 mm to 105 mm. It was observed that the value of S_{11} decreased.

Figure 6: Reflection curves for tuning the gap of slit top : W = 7.5 mm, w_p = 6 mm, h = 1.6 mm, ε_r = 4.4, (a) w_g is varied from 0.4 to 1.4 mm, (b) w_p is varied from 4.5 to 6.5 mm (w_g=0.8 mm. is Fixed), and (c) D is varied from 65 to 105 mm.

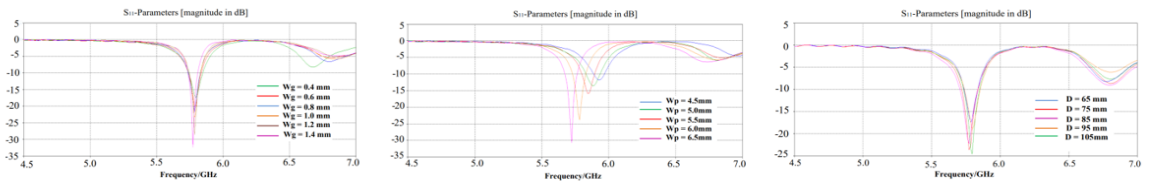

(a) (b) (c)

Table 1: Shows parameters of the dual beam antenna diameters (D) is Varied from 45 to 95 mm.

Parameters of Dual Beam Antenna						
Substrate and Ground (D)	95 mm	85 mm	75 mm	65 mm	55 mm	45mm
Frequency	5.8 GHz	5.8 GHz	5.8 GHz	5.8 GHz	5.8 GHz	5.8 GHz
Gian	7.53 dB	6.63 dB	7.13 dB	6.75 dB	5.80 dB	5.34 dB
Main Beam direction	50°	40°	35°	40°	45°	45°
Half power beamwidth	46° (31°-77°)	61.1° (14.5°-76.6°)	52.4° (17.2°-69.7°)	52.8° (18.7°-71.5°)	57.2° (20.3°-77.5°)	59.2° (21.5°-80.7°)
Side lobe level	-7.0 dB	-8.2 dB	-9.1 dB	-8.7 dB	-7.5 dB	- 6.7dB
Total efficiency	-0.095 dB	-0.149 dB	-0.075 dB	-0.033 dB	-0.168 dB	-0.143 dB
Null beam width between dual-beam	32°	17°	16°	18°	22°	10°

As shown in Table 1, the main beam direction and half-power beamwidth depend on the antenna diameter, resulting in a change in the angle by varying the antenna diameter (D) from 45 to 95 mm. When reducing the width D by 10 mm steps, it can be observed that the gain is reduced, but the degrees of the main beam direction and half-power beamwidth are increased, which is very useful for extending the flight range of UAVs. The 75 mm of substrate and ground are suitable diameters for the design of the beam-steering antennas at a constant tilted beam of 35° and angular width (3 dB) of 52.4° (17.2°-69.7°) in the elevation plane.

Table 2: Shows the binary code of PIN diode is a suitable position.

Number	**D_1**	**D_2**	**D_3**	**D_4**	**D_5**	**D_6**	**D_7**	**D_8**	**Direction**	**Main lobe direction**	
										Azimuth	**Elevation**
1	L	H	H	H	L	H	H	H	90°	90°	-35°
2	H	L	H	H	H	L	H	H	45°	45°	35°
3	H	H	L	H	H	H	L	H	0°	0°	-35°
4	H	H	H	L	H	H	H	L	135°	135°	35°

Figure 7: Shows (a) A dual beam- steering antennas model (b) 3D elevation plane (c) 3D azimuth (d) the reflection coefficients (e) the pattern of elevation plane, and (f) the pattern of azimuth plane.

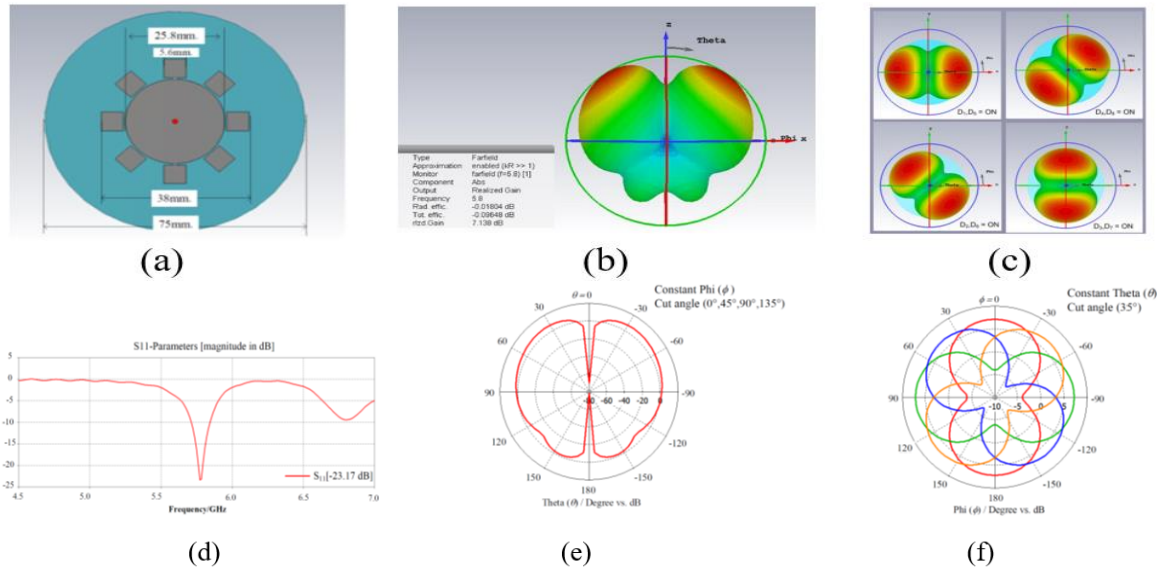

The antenna operates on the 5.8 GHz test frequency band and covers the C-band. The eight small square patches were arranged symmetrically with respect to the center of the antenna, and the center circular patch was fed coaxially. When two small square patches opposite each other are activated, and the feed point of the remaining small square patch is an open circuit by the PIN diode, which is explained by the binary code of the pin diode position shown in Table 2, is a suitable position for the bias pin diode and shows binary code control steering beams. The simulation results for the reflection coefficients of the dual beam-steering antennas using a metasurface formed by a small square patch are shown in Figure 7(a). The simulation results of the 3D patterns for the elevation and azimuth planes show that the antenna provides a gain of 7.13 dB in Figures 7(b-c). We found that the proposed antenna is able to retain the frequency bandwidth minimum 113 MHz [5.737 GHz to 5.850 GHz] around 5.8 GHz at S_{11}= -23.17 dB in Figure 7(d). The antenna generates a tilted beam of 35° in all elevation planes and a rotated dual beam at each 45° azimuth plane, as shown in Figure 7(e-f). The antenna can switch the tilted beam in eight directions on the space quadrants in the azimuth plane by exciting forward bias pin diodes in the space quadrants, which are binary sequences. This antenna is capable of steering its dual beam (1st and 2rd beams) to 0° with 180°, 45° with -135°, 90° with -90°, and 135° with -45° angles and an angular width of 96° at 3 dB in the azimuth plane, which is sufficient for pattern overlapping, as shown in Figure 7(f).

Simulation Results of Antenna with Meta Radome

This section presents the simulation results for an antenna with a meta-radome. Starting by simulating each unit cell type at the center frequency f_c of 5.8 GHz, to analyze the characteristics of the metamaterial structure, the S-parameters were extracted to calculate the effective permittivity (ε_{eff}) and effective permeability (μ_{eff}), which are derived as follows (Kamonsin et al., 2020):

$$\varepsilon_{eff} = \frac{2}{jkh} \times \left(\frac{1-(S_{21}+S_{11})}{1+(S_{21}+S_{11})} \right) \quad (20)$$

$$\mu_{eff} = \frac{2}{jkh} \times \left(\frac{1-(S_{21}-S_{11})}{1+(S_{21}-S_{11})} \right) \quad (21)$$

Figure 8: Shows the magnitudes of (a) Simulated results of S_{11} and S_{21} for SL-FSS and JC-FSS (b) S_{11} of SL-FSS, JC-FSS and Combined JC-FSS with SL-FSS. (c) S_{11} of g_2 is varied from 0.4 to 1.2 mm, and (d) the simulated results of S_{11} and S_{21} for JC-FSS with SL-FSS.

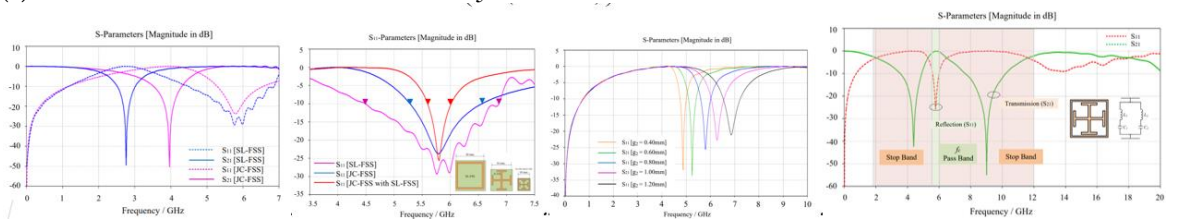

where S_{11} is the reflection coefficient, S_{21} is the transmission coefficient, h is the substrate thickness, and k is the wave-number. Using CST simulation software, which is based on the finite element method, the geometric parameters of Our proposed unit cells, printed on a FR4 substrate ($\varepsilon_r = 4.4$, $tan\delta = 0.025$) was defined as the JC-FSS combined SL-FSS with dimensions of D = 75 mm, d_1 = 10 mm, d_2 = 4.2 mm, p = 11.8 mm, w_1 = 0.55 mm, w_2 = 0.6 mm, g_1 = 1.8 mm, g_2 = 0.8 mm and h = 1.6 mm Figure 5(a), which is more compact by almost 1/3 compared to conventional SL-FSS and JC-FSS structures, see Figure 8(a) shows the simulated results of S_{11} and S_{21} for SL-FSS and JC-FSS, which both characterize the bandpass filter at f_c 5.8 GHz as observed in the LC equivalent circuit which provides a transmission coefficient S_{21} of band stops at f_r 2.76 GHz and 3.96 GHz frequencies, respectively. They both have a bandpass bandwidth, which is wider than the combination of JC-FSS with SL-FSS, but they both have a large size. Consider Figure 8(b) shows the simulated results of S_{11} for different types of unit cells, in which the combination of JC-FSS with SL-FSS can reduce the size of the meta radome is decreased, see Figure 8(c) shows S_{11} of g_2 is varied from 0.4 to 1.2 mm, the values of L and C decrease, which is assigned to characterize the reflection curve that occurs in the required frequency band and Figure 8(d) shows the simulated reflection coefficient S_{11} and transmission coefficient S_{21} of JC-FSS with SL-FSS, which characterize the bandpass filter at f_c 5.8 GHz, 425 MHz of bandwidth as observed in the $L_1C_1//L_2C_2$ equivalent circuit, which provides a transmission coefficient S_{21} of two band stops at 4.4 GHz and 9.0 GHz frequencies, the bandwidth of the pass band can be increased by increasing the distance of a gap (g).

Figure 9: Shows the multilayer of Combined JC-FSS with SL-FSS and Simulated results of S_{11} for the unit cell distance arrangement.

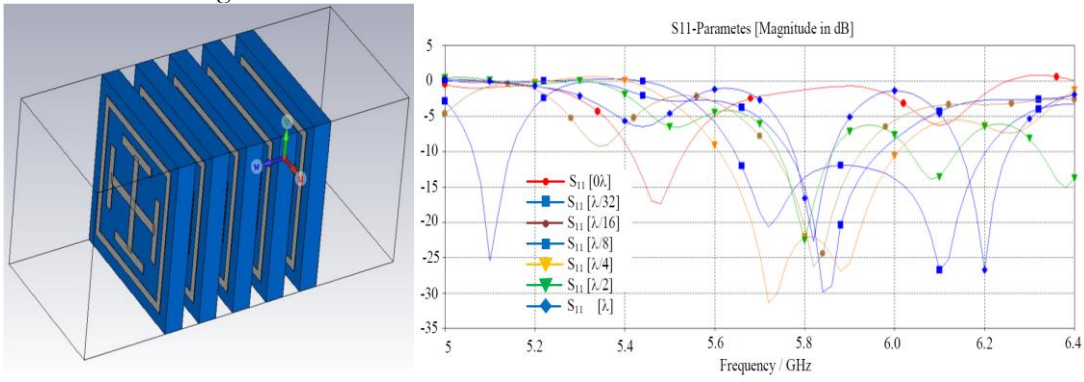

Figure 9 shows the multilayer of the combined JC-FSS with a conventional SL-FSS. The air-gap distance (λ) between each unit cell directly influenced the bandwidth of S_{11}. Any air gap distance can increase the gain of the antenna except when the air gap distance is zero, but we chose a distance between the air gap and h of ($\lambda/4$) for a dual-beam antenna, which provides a high gain, and the propagation pattern has the least distortion.

We may describe the properties of the material at the macro level with the parameters of electrical permittivity and magnetic permeability (ε and μ, respectively), both parameters (Spada, 2017). This can be grouped into groups of materials, as shown in Figure 10(a), in which the metamaterial-based radome is near zero (ε = 0.0142 and μ = 0.0134, respectively), as shown in Figure 10(b). It is the NZI for wave propagation in 1st quadrants of terminology and classification.

Figure 10: Shows (a) Terminology and classification, and (b) Tables of permittivity and permeability.

Figure 11: Simulated results of dual beam-steering antennas with a meta radome (a) 3D antennas structure with a meta radome (b) Elevation plane and (c) Azimuth plane, and (d) simulated results of far field for antennas installed on two wings of an aircraft.

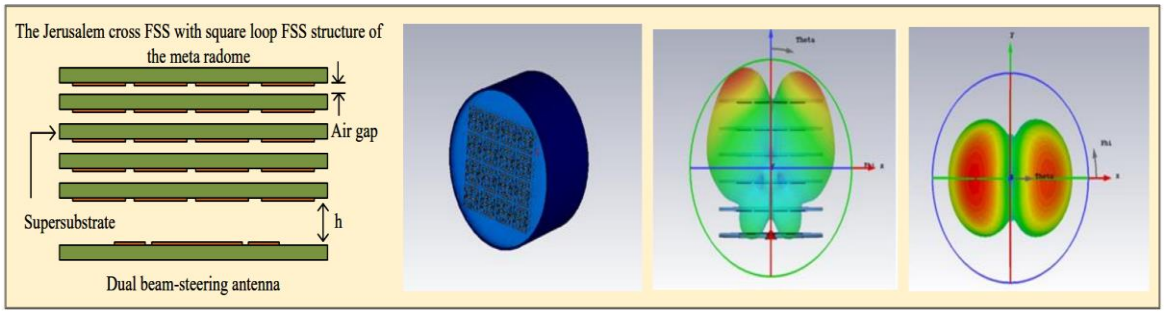

Figure 11 shows the simulated results of the dual beam-steering antennas with a meta-radome. Figure 11(a) shows the 3D structure of the antennas with a meta-radome. The microstrip antenna was grounded

at the bottom, and the meta radome was placed on top of a mirror plate with a very high reflection coefficient and two parallel plates at a reasonable distance (typically half the wavelength). The air gap can be adjusted by the wavelength ratio (Chun-Yih et al., 2007; Foroozesh, & Shafai, 2010; Tanan et al., 2018). If the air gap narrows at the appropriate wavelengths, the meta-radome increases the antenna gain. For the design and experiment, we selected a distance between the air gap and h of ~12.9 mm. ($\lambda/4$), which provides high gain, and the propagation pattern has the least distortion. In particular, the angle of the tilted beam must be at the same position or must have the least deviation. Figure 11(b) gain of the antenna to increase when increasing the number of the meta radome which gains are 7.65 dB at 1 Layer, 7.93 dB at 2 Layers, 8.40 dB at 3 Layers, 9.51 dB at 4 Layers and 10.18 dB at 5 Layers in Elevation plane and Figure 11(c) Azimuth plane. Finally, Figure 11(d) shows the simulation results at ϕ = 0° for the far field of the antennas installed on the two wings of an aircraft. The coupling fields of the two antennas, cause the propagation to cover the entire area according to the elevation angle. Steering according to the azimuth angle will result in waves covering all directions, and the gain of the antennas is increased by approximately 2 dB, corresponding to (Muhammad et al., 2011).

Fabrication and Test

A prototype of the proposed structure was fabricated to test and validate the simulation results, as shown in Figure 12. Figure 12 shows (a) the front of the dual beam-steering antenna with a PIN diode connected between the circular patches and square patches, (b) the back of the dual beam-steering antenna with holes drilled for copper wires to connect to the controller, and Figure 12(c) the prototype of 4 × 4 unit cells for the fabricated meta-radomes. The proposed unit cells were printed on an FR4 substrate (ε_r = 4.4, $tan\delta$ =0.025, h=1.6 mm).

Figure 12: Shows (a) the front of the dual-beam steering antenna (b) the back of the dual-beam steering antenna, and (c) the prototype of meta radomes.

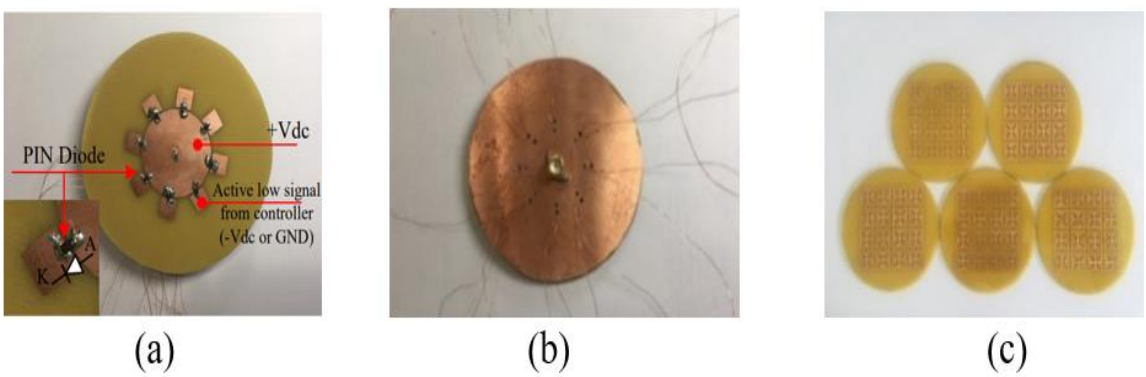

PIN Diode Driver Printed Circuit Board.

A prototype of the proposed structure for testing and controlling PIN Diode switches according to the designed circuit, as shown in Figure 2, was fabricated, as shown in Figure 13(a). The PIN diode driver printed circuit board consists of the following devices: chip inductor (L_2) is 47 nH, resistor (R_L) is 100 Ω, and chip resistor (R_1) is ≤ 430 Ω, Figure 13(b) shows the bias tee Modul. For forward biasing the diode, a 5 V DC power supply is required. A current of 50 mA was set for the bias T module, and 10 mA for the pin diodes. The RF transmittance measurements, the results of which are shown in Figure 13(c) and (d), were compared between the factory value and the measurement value, and it can be seen that the PIN diode was transmitted completely.

Figure 13: Shows (a) PIN Diode printed circuit bord, (b) Bias tee Modul, (c) The insertion loss of PIN diode for forward bias, and (d) The return loss of PIN diode for forward bias.

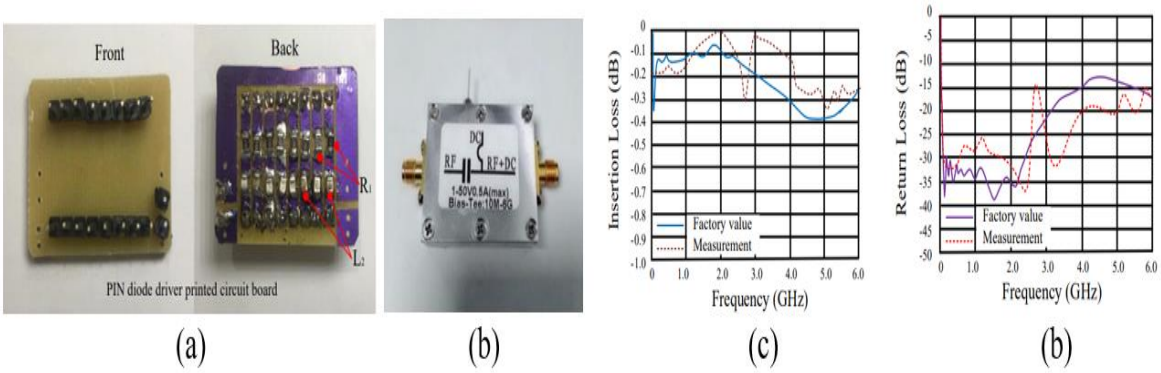

The Measurement Setup for Fabricated Dual Beam Antenna

To characterize the reflection and transmission coefficients of a dual-beam steering antenna. The measurement setup is shown in Figure 14(a). A prototype of the dual-beam steering antenna was assembled and tested in a semi-acoustic chamber at Telecommunications engineering laboratory, Suranaree University of Technology, Thailand. The receiving and transmitting antennas are located at a distance in the far-field region for measuring S_{11} and S_{21} of the dual-beam steering antenna, which is connected to port 1 of a vector network analyzer, whereas the receiving ultra-wideband tapered slot antenna is connected to port 2.

Figure 14: Shows (a) The measurement setup for fabricated dual beam antenna (b) S_{11} of simulation with measurement (c) radiation patterns in elevation plane (d) radiation patterns in azimuth plane at 0º, 90º, and (e) radiation patterns in azimuth plane at 45º, -45º.

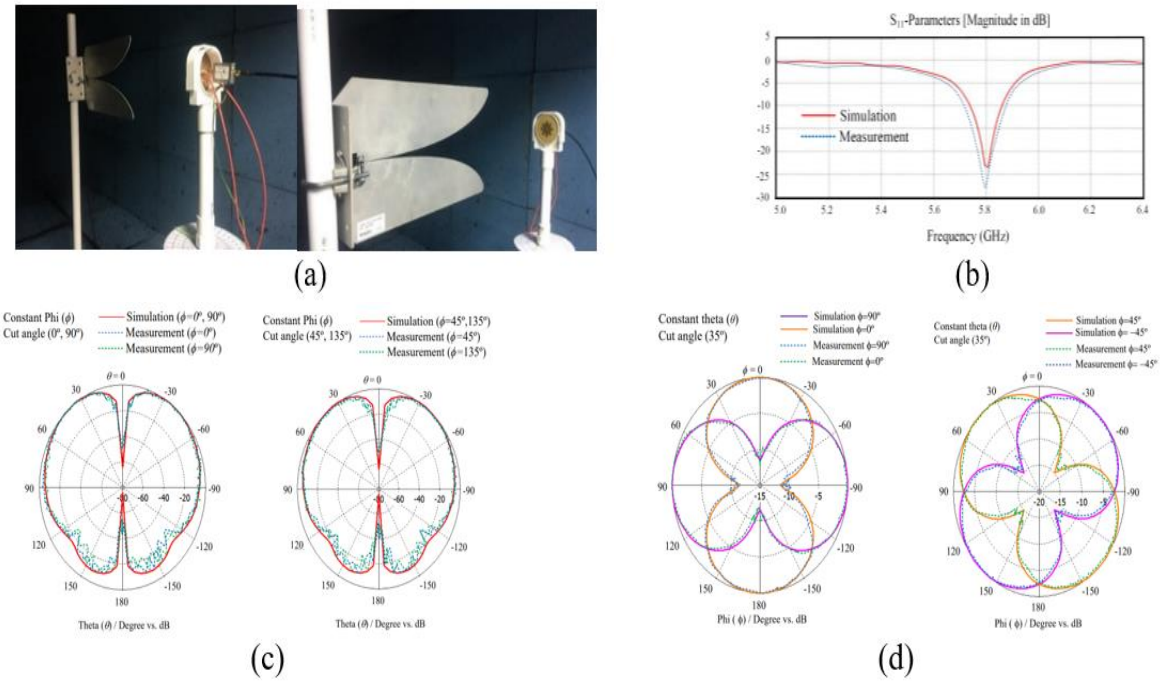

A simulation with the measurement results of the reflection coefficients (S_{11}) of the dual beam-steering antennas is shown in Figure 14(b). We found that the proposed antenna is able to retain the frequency bandwidth minimum 113 MHz [5.737 GHz to 5.850 GHz] around 5.8 GHz at S_{11}= -23.17 dB and gain is 7.13 dB. Figure 14(c-d) shows measured radiation patterns in elevation plane and azimuth plane are S_{11} = -28.5 dB and gain are 7.21 dB at 0º, 90º and gain are 7.18 dB at 45º, -45º and the frequency bandwidth is ~134 MHz [5.722 GHz to 5.856 GHz]. It provides a constant tilted beam of 35° with an angular width of 50° (19°–69°) in the elevation plane, and an angular width of ~ 94° at 3 dB in the azimuth plane.

Figure 15: A prototype of proposed structure for testing antenna with the multi-layer radomes.

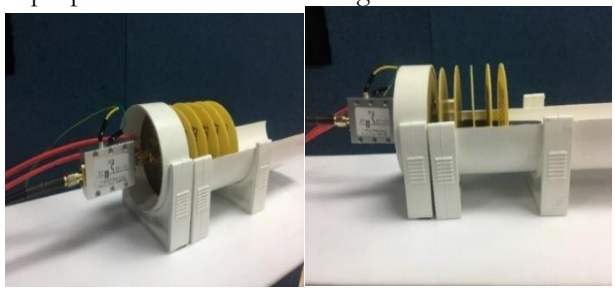

Finally, for the design and experiment, we selected a distance between the air gap and *h* of ~12.9 mm. ($1/4\lambda$), which provides high gain, and the propagation pattern has the least distortion. Figure 15 shows a prototype of the proposed structure for testing the antenna with the super-substrate multi layer meta-radomes by stacking five meta-radomes at a spacing of 12.9 mm, which improves the efficiency of the electronically steered dual-beam antenna.

Figure 16: Shows (a) The measurement setup for fabricated dual beam antenna with meta radome (b) S_{11} parameter of antenna with meta radome (c) radiation patterns in elevation plane, and (d) radiation patterns in azimuth plane at 0º, 90º and azimuth plane at 45º, -45º.

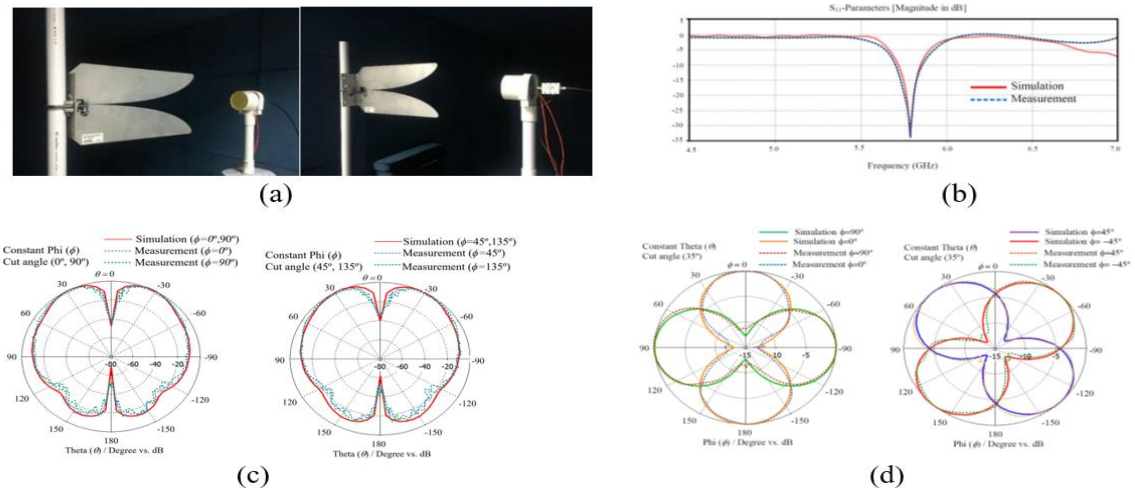

The measurement setup for the fabricated dual-beam antenna with a meta-radome of a combined JC-FSS with a conventional SL-FSS is shown in Figure 16(a)**.** The simulation results for the reflection coefficients of the dual beam-steering antennas using a metamaterial-based radome are shown in Figure 16(b). We found that the proposed antenna is able to retain the frequency bandwidth minimum 125 MHz [5.729 GHz to 5.854 GHz**]** around 5.8 GHz at S_{11} = -33.5 dB and gain is 10.18 dB. Figure 16(c-d)

shows measured radiation patterns in elevation plane and azimuth plane measured radiation patterns in the elevation plane and azimuth plane are S_{11} = -33.8 dB and gain are 10.23 dB at 0º, 90,º and gain is 10.19 dB at 45º, -45º and the frequency bandwidth is ~138 MHz [5.724 GHz to 5.862 GHz]. While It provides a constant tilted beam of 35° with an angular width of 40° (15°-55°) at 3 dB in the elevation plane, and an angular width of ~74° at 3 dB in the azimuth plane, which is sufficient for pattern overlap.

Conclusion

A technique for enhancing the gain of an electronically steered dual-beam antenna using a metamaterial radome operates over a test frequency band of 5.8 GHz, with bandwidths of approximately 113 MHz (at -10 dB), which covers the C-band, which is high enough for the UAVs applications, such as antennas installed on two wings of an aircraft that can be tracked or commanded from its control station within a given range and without disconnection. This antenna can increase or decrease the beam width at the elevation angle by adjusting the diameter of the dielectric and ground, expandable 35°-50° of the main beam direction and 59.2°(21.5°-80.7°) of the maximum half-power beam width. If applied to a single beam antenna, the gain can be increased by more than 3 dB by using only one to three layers of meta-radomes or fewer than five layers. Our antennas can provide higher gain than antennas arranged with the unit cell array in the same plane and a typical UAV antenna has a gain of only ~ 4-7 dB. The designed meta-radome can be applied to a variety of antennas and will provide high gain and accurate beam direction with very little error. Eight square patches were arranged symmetrically with respect to the center of the antenna, and the center circular patch was fed coaxially. When activating two small square patches opposite to each other and the feed point of the remaining small square patch is an open circuit by the PIN diode or terminated at 50 Ω impedance, the antenna is investigated at 5.8 GHz of frequency, which generates a tilted beam of 35° in the elevation plane. While the antenna provides a gain of ~7.21 dB without a radome and ~10.23 dB with a meta-radome, the frequency bandwidth is ~138 MHz around 5.8 GHz. This antenna is capable of steering its dual beam (1st and 2nd beams) to 0° at 180°, 45° at -135°, 90°at -90°, and 135°at -45° angles. The antenna can switch dual beams in eight different space quadrants in the azimuth plane by exciting forward bias pin diodes in the space quadrants. The binary sequence, in which the antenna has permittivity and permeability, is near zero (ε = 0.0142 and μ = 0.0134), respectively.

Acknowledgement

This work was supported by the Research Department Institute of Engineering, Suranaree University of Technology, Nakhon Ratchasima, Thailand.

References

Asaduzzaman Towfiq Md., Israfil Bahceci, Sebastian Blanch , Jordi Romeu, Lluis Jofre, & Bedri A. Cetiner. (2018). A reconfigurable antenna with beam steering and beamwidth variability for wireless communications. *Transactions on antennas and propagation*, 66(10), October 2018. https://ieeexplore.ieee.org/document/8410614

Anderson, I. (1975). On the theory of self-resonant grids. *The bell system technical journal*, 54(10), USA, December 1975. https://ieeexplore.ieee.org/document/6778870

Bahl, I. (2003). Lumped elements for RF and microwave circuit. *Norwood. Artech House, Inc.*, UK.

Balanis, C. A. (2005). Antenna Theory-Analysis and Design. *John Wiley and Sons*, (817-821).

Camblor, R., Ver Hoeye, S., Hotopan, G., Vazquez, C., Femandez, M., & Heras, A.F. (2010). Design of a submillimeter microstrip array for beam scanning applications. *IEEE Proceedings*. https://ieeexplore.ieee.org/document/5612340

Chun-Yih Wu, Shih-Huang Yeh & Tzu-Hao LuPlanar. (2007). Novel high gain metamaterial antenna radome for WiMAX operation in the 5.8-GHz band. *IEEE Proceedings*. https://ieeexplore.ieee.org/document/4396289

Defence Technology Institute. (2016). Annual Report 2016. *Ministry of Defiance. the Kingdom of Thailand*. https://www.dti.or.th/download/file/82d26e2b.pdf

Engheta, N., & Ziolkowski, R.W. (2006). Metamaterials: physics and engineering explorations. *John Wiley & Sons*, *Inc*: USA.

Foroozesh, A. & Shafai, L. (2010). Investigation into the effects of the patch type fss superstrate on the high-gain cavity resonance antenna design. *IEEE Transaction Antenna propagation*, 58(2), 258-270. https://ieeexplore.ieee.org/document/5345759

Government Gazette. (2018). Rules and conditions of unmanned aerial vehicle (UAV) radio frequency license for general use. *The Office of the National Broadcasting and Telecommunications Commission*, Volume 135 Special Part 11 Ngor.

Gupta, K. C., Garg, R., Bahl, I., & Bhartia, P. (1996). Microstrip lines and slot-lines. *Norwood: Artech House*. 2nd ed.

Hisamatsu Nakano, Tomoki Abe, & Junji Yamauchi. (2017). Beam-steering antennas using metalines. *ISAP2017*, Phuket, Thailand. https://ieeexplore.ieee.org/document/8228725

Hosseini, M., & Hakkak, M. (2008). Characteristics estimation for Jerusalem cross-based artificial magnetic conductors. *IEEE Antenna and Wireless Propagation Letters* (pp. 58-61). IEEE. https://ieeexplore.ieee.org/document/4444743

Iyemeh Uchendu & James Kelly. (2016). Survey of beam steering- techniques available for millimeter wave applications. *Progress In Electromagnetics Research B*, 68, 35–54. https://www.jpier.org/issues/volume.html?paper=16030703

Jais, M.I., Jamlos, M., Sabapathy, T., & Kamarudin. (2013). 2.45 GHz beam -steering textile antenna for WBAN application. *IEEE Proceedings*. https://ieeexplore.ieee.org/document/6710761

Kamonsin, W., Krachodnok, P., Chomtong, P., & Akkaraekthalin, P. (2020). Dual-band metamaterial based on jerusalem cross structure with interdigital technique for LTE and WLAN systems. *IEEE Access*. https://ieeexplore.ieee.org/document/8966338

Muhammad Ezanuddin, A.A., Malek, F. and Soh, P.J. (2011). Development of a complementary split ring resonator antenna," *Lap Lambert Academic Publishing*. USA.

Pristin K Mathew. (2013). Optimization of Jerusalem cross frequency selective surface. *International Journal of advanced research in Electronics and Communication Engineering*, 2(12), 947-950.

Parker, E.A. (1991). The gentleman's guide to frequency selective surfaces. *Presented in 17th Q.M.W. Antenna Symposium*, London, UK. https://www.researchgate.net/publication/266338883

Sievenpiper, D. (1999). High-impedance electromagnetic surfaces. *Ph.D. dissertation*, Univ. Calif., Los Angeles.

Simovski, C. R., Maagt, P. D., & Melchakova, I. V. (2005). High impedance surfaces having stable resonance with respect topolarization and incidence angle. *IEEE Transaction on Antennas Propagation*, 53(3), 908-914. https://ieeexplore.ieee.org/document/1406219

Spada, L.L. (2017). "Metamaterial for advanced sensing platforms," *Journal of optics technology letters,* 35(1), 47-51. https://www.scitechnol.com/peer-review/metamaterials-for-advanced-sensing-platforms-aveC.php?article_id=6851

Tanan, H., Sarawuth, C., Prayoot, A., & An Zhao, Y. (2018). Design of compact beam-steering antennas using a metasurface formed by uniform square rings. *IEEE Access, special Section on tunable devices for modern communications*, 1-10. https://ieeexplore.ieee.org/document/8272328

Xinhuan Yang, Yanzhu Qi, Bo Yuan, Yazi Cao, & Gaofeng Wang (2021). A miniaturized high-gain flexible antenna for UAV applications. *International Journal of Antennas and Propagation*. 2021, 1-7. https://doi.org/10.1155/2021/9919425

Yang, F., & Rahmatsamii, Y. (2009). Electromagnetic band gap structures in antenna engineering," *Cambridge*, UK.

Yuan Xu & Mang He, (2019), Design of multilayer frequency-selective surfaces by equivalent circuit method and basic building blocks. *International Journal of Antennas and Propagation*, 2019, 1-13. https://doi.org/10.1155/2019/9582564

Zhang Wei & Yang Junfeng, (2017), A Design of Vertical Polarized Conformal Antenna and Its Array Based on UAV Structure. *International Journal of Antennas and Propagation,* 2017, 1-12. https://doi.org/10.1155/2017/9769815

Zhang Wei & Yang Junfeng, (2018), Design of L-Shaped Open-Slot Antenna Used in UAV Airborne Communication System. *International Journal of Antennas and Propagation*, 2018, 1-13. https://doi.org/10.1155/2018/6846193